

Modeling gas-phase nucleation in inductively coupled silane-oxygen plasmas

S.-M. Suh, S. L. Girshick,^{a)} and U. R. Kortshagen

Department of Mechanical Engineering, University of Minnesota, Minneapolis, Minnesota 55455

M. R. Zachariah

Department of Mechanical Engineering and Department of Chemistry, University of Minnesota, Minneapolis, Minnesota 55455

(Received 14 June 2002; accepted 28 October 2002; published 19 December 2002)

A detailed chemical kinetics mechanism was developed to model silicon oxide clustering during high density plasma chemical vapor deposition of SiO₂ films from silane-oxygen-argon mixtures. An inductively coupled plasma reactor was modeled in a one-dimensional multicomponent two-temperature framework. Spatial distributions of species concentrations were calculated. The effects of discharge parameters and the main processes contributing to cluster formation were examined. A sensitivity analysis was conducted to determine the dominant reactions that affect the model results. © 2003 American Vacuum Society. [DOI: 10.1116/1.1531143]

I. INTRODUCTION

Recently high density plasma (HDP) processing has become increasingly popular in the microelectronics fabrication industry, because one can achieve high deposition rates at low wafer temperatures while also having the capability of anisotropic deep etching. Inductively coupled plasmas (ICPs) are widely used as HDP source for various thin film deposition and etching processes. Although the operating pressure of a typical HDP chemical vapor deposition (CVD) process is maintained very low (5–20 mTorr), some experimental studies^{1–3} indicated that gas-phase nucleation of contaminant particles can be a problem in many of these processes. This problem will become more severe as the “critical size of killer particles” decreases along with the characteristic feature size, which is projected to be about 50 nm by 2003.⁴ It thus becomes increasingly important to improve our understanding of the kinetics of particle nucleation, growth, and transport in HDP environments. Moreover, the development of experimentally verified numerical models will provide a valuable tool for cost-effective process screening and optimization.

To our knowledge no previous study has reported the development of a detailed model for clustering and particle nucleation in low-pressure silane-oxygen plasmas. Mandich and Reents⁵ investigated the growth of large cationic clusters in the presence of silane-water mixtures, since water contamination in silane plasmas has been a concern. They demonstrated sequential growth of large clusters starting with a subsilane cation and concluded that low levels of water contamination can lead to the generation of macroscopic dust particles. Hollenstein *et al.*² used infrared absorption spectroscopy and mass spectrometry in an experimental study of particle formation in a capacitively coupled silane-oxygen-argon plasma. Anions of high mass were observed whereas neutrals and cations were detected at lower mass ranges. A few theoretical and experimental studies^{6,7} examined the

postoxidation of silicon films on the surfaces of existing silicon particles.

The modeling of inductively coupled HDP discharges in the absence of particle nucleation has been relatively well studied,^{8–13} but no model has previously been reported that treated both particle nucleation and a spatially varying plasma structure. Bhandarkar *et al.*¹⁴ developed a detailed nucleation model for a pure silane plasma, but that model was zero dimensional, and treated species diffusion only in an approximate way as a sink term in the species population equations. Meeks *et al.*^{15,16} developed a detailed model for plasma chemistry in the silane-oxygen-argon system, with 46 neutral and ionic gas species together with 13 surface species participating in over 200 reactions under HDP conditions.¹⁵ This work adopted a zero-dimensional perfectly stirred reactor approach, which allows computational efficiency by eliminating the consideration of species transport.

To our knowledge no model currently exists, for any chemical system, that satisfactorily accounts for detailed chemical clustering that leads to particle nucleation, while also considering species transport in a plasma discharge with physical dimensions. In this work, a fundamental kinetic approach is represented to model homogenous nucleation of silicon oxide particles in an inductively coupled silane-oxygen plasma reactor. A detailed chemical clustering mechanism was developed that extends the neutral silicon oxide clustering mechanism presented by Suh *et al.*¹⁷ An ICP reactor was modeled by constructing a set of one-dimensional conservation equations for mass, momentum, and energy within a multicomponent two-temperature framework. The clustering mechanism was self-consistently coupled to the reactor model, and time-dependent one-dimensional (1D) simulations were conducted for a variety of discharge parameters.

II. SILICON OXIDE CLUSTERING MECHANISM

The base gas-phase reaction mechanism for SiH₄-O₂-Ar plasma chemistry was adopted from the work of Meeks *et al.*¹⁵ The clustering mechanism presented here

^{a)}Electronic mail: slg@umn.edu

TABLE I. Summary of the clustering reaction types and rate constants in silane-oxygen-argon plasmas.

	Reaction type	Prototypical reactions ^a	k_f (cm ³ s ⁻¹) ^b	
	1	Attachment	$e + (\text{SiO}_x)_n^- \rightarrow (\text{SiO}_x)_{n+1}^-$	$8.6 \times 10^{-6} T_e^{0.5}$
	2	Dissoicative attachment	$e + (\text{SiO}_x)_n^- \rightarrow (\text{SiO}_x)_{n-1}^- + \text{SiO}_x$	c
	3	Ionization	$e + (\text{SiO}_x)_n^- \rightarrow (\text{SiO}_x)_n^+ + 2e$	$1.2 \times 10^{-39} T_e^{6.365}$
Electron impact reactions	4	Dissociation	$e + (\text{SiO}_x)_m \rightarrow (\text{SiO})_m + m\text{H}_2 + e$	$2 \times 10^{-2} T_e^-$ ${}^1 \exp(1.2 \times 10^5 / T_e)$
	5	Dissociation	$e + (\text{HSiOOH})_m \rightarrow (\text{SiO}_2)_m + m\text{H}_2 + e$	$2 \times 10^{-2} T_e^-$ ${}^1 \exp(1.2 \times 10^5 / T_e)$
	6	Electron detachment	$e + (\text{SiO}_x)_n^+ \rightarrow (\text{SiO}_x)_n + 2e$	$1.58 \times 10^{-10} n^{2/3} T_e^{0.5}$
	7	Radiative recombination	$e + (\text{SiO}_x)_n^+ \rightarrow (\text{SiO}_x)_n + h\nu$	$1.1 \times 10^{-11} T_e^{0.5}$
	8	Dissociative recombination	$e + (\text{SiO}_x)_n^+ \rightarrow (\text{SiO}_x)_{n-1} + \text{SiO}_x$	$1.1 \times 10^{-5} T_e^{0.5}$
Mutual neutralization	9	Neutralization	$(\text{SiO}_x)_n^{+/-} + \text{A}^{-/+} \leftrightarrow (\text{SiO}_x)_n + \text{A}$	$2 \times 10^{-6} T^{-0.5}$
	10	Associative neutralization	$(\text{SiO}_x)_j^{+/-} + \text{B}^{-/+} \leftrightarrow (\text{SiO}_x)_j \text{B}$	$2 \times 10^{-6} T^{-0.5}$
Clustering reactions	11	Ion-Neutral clustering	$(\text{SiO}_x)_n^{+/-} + (\text{SiO}_x)_l \leftrightarrow (\text{SiO}_x)_{n+l}^{+/-}$	$2 \times 10^{-9} (\alpha/m_r)^{0.5}$
	12	Self-clustering	$(\text{SiO}_x)_n + (\text{SiO}_x)_l \leftrightarrow (\text{SiO}_x)_{n+l}$	d
	13	SiO addition	$(\text{SiO})_n + (\text{SiH}_2\text{O})_m \rightarrow (\text{SiO})_{n+m} + m\text{H}_2$	d
	14	SiO ₂ addition	$(\text{SiO}_2)_n + (\text{HSiOOH})_m \rightarrow (\text{SiO}_2)_{n+m} + m\text{H}_2$	d

^a $n \leq 11$, $l \leq 11$, $n+l \leq 11$, $x=1$, or 2 , $m=1$ or 2 , $n+m \leq 11$, and $j \geq 4$. A is an ionic molecule. B is another cluster.

^b T_e and T are, respectively, the electron and ion temperature in kelvin. α is the polarizability of the neutral and m_r is the reduced mass.

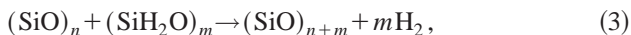
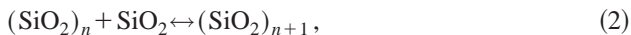
^c 2×10^{-11} for $n=2$, 2×10^{-12} for $n=3$, and 2×10^{-13} for $n \geq 4$.

^dThe rate parameters can be found in Ref. 8.

for a high-density SiH₄-O₂-Ar plasma extends the model for neutral clustering during low-pressure silane oxidation previously developed by Suh *et al.*^{17,18} Given the complexity inherent in the Si-H-O system, and the enormous potential number of Si_xH_yO_z species, our approach considers clustering only by those silicon-containing species that are believed most likely, under these conditions, to cluster, and that are predicted to exist in sufficient abundance to play a potentially important role in clustering. The mechanism includes clusters containing up to 11 silicon atoms. Further growth of clusters beyond this size is not considered here, and, once formed, clusters containing more than 10 silicon atoms are assumed to be chemically nonreactive.

A. Reaction types and rate parameters

A detailed description of the neutral clustering mechanism is provided in our previous work.¹⁷ The neutral clustering mechanism consists of the following four classes of reactions: the reversible self-clustering of SiO and SiO₂, together with contributions from SiH₂O and HSiOOH and their dimers:

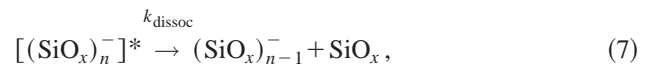
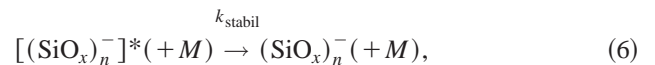
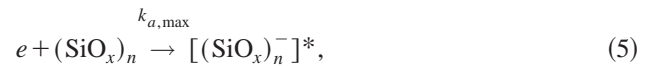


for $1 \leq n \leq 9$, $m=1$ or 2 , and $n+m \leq 10$.

This neutral clustering mechanism is extended to include the following classes of reactions that are expected to be important in HDP environments: (1) electron-impact reactions with neutral and charged clusters of SiO, SiO₂, SiH₂O, and HSiOOH; (2) mutual neutralization of charged clusters; and (3) clustering reactions between neutral and charged spe-

cies. Reaction types and rate parameters are summarized in Table I. The resulting mechanism, including both the base mechanism and clustering reactions, contains 104 species participating in 523 reactions.

Electron-impact reactions include eight prototypical reaction types. Since silicon oxides have positive electron affinities, electron attachment reactions (reaction type 1) can play an important role:



where M is a third body and $x=1$ or 2 . In reaction (5), it is assumed that the excited anionic cluster $[(\text{SiO}_x)_n^-]^*$ is structurally large and stable with a number of multiple bonds. This assumption can lead to further simplification such that autodetachment of the electron [reverse direction of reaction (5)] is negligible and that the stabilization process, reaction (6), is dominant over the dissociation process, reaction (7). The overall nondissociative reaction rate, therefore can be approximated to be $k_a \approx k_{a,\max}$, and is obtained based on the maximum (*s*-wave) electron-capture cross section.¹⁹

$$\sigma_{\max} = \pi \left(\frac{\lambda_B}{2\pi} \right)^2 = \frac{1.197 \times 10^{-15}}{\epsilon(\text{eV})} \text{ (cm}^2\text{)}, \quad (8)$$

where λ_B is the deBroglie wavelength of the electron and ϵ is the electron energy. The overall cross section of the dissociative attachment reaction (reaction type 2) can be roughly estimated to be $10^{-18} - 10^{-20}$ cm².²⁰

For the reactions whose collision cross sections are known, the rate coefficients are calculated by assuming that the electron energy distribution function (EEDF) is Maxwellian:

$$k_i = \left(\frac{8}{\pi m_e} \right)^{1/2} \left(\frac{1}{k_B T_e} \right)^{3/2} \int_0^\infty \epsilon \sigma_i(\epsilon) \exp\left(-\frac{\epsilon}{k_B T_e}\right) d\epsilon, \quad (9)$$

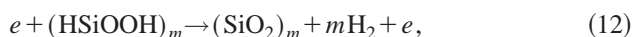
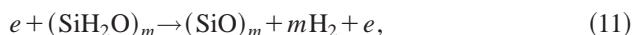
where $\sigma_i(\epsilon)$ is the electron-energy-dependent cross section of the i th reaction, m_e is the electron mass, k_B is the Boltzmann constant, T_e is the mean electron temperature, and k_i is the integrated rate coefficient of the i th reaction.

Ionization of silicon oxide clusters (reaction type 3) can take place when the electron energy is higher than the ionization potential (IP). Electron-energy-dependent ionization cross sections are used in the following semiempirical form:²¹

$$\sigma_{\text{ionization}} = \sigma_{\text{max}} 2.72 \left(\frac{\text{IP}}{\epsilon} \right) \log\left(\frac{\epsilon}{\text{IP}}\right), \quad (10)$$

where σ_{max} is the maximum electron-capture cross section given in Eq. (8).

Electron-impact dissociation reactions of SiH_2O and HSiOOH and their dimers (reaction types 4 and 5), that produce SiO and SiO_2 , respectively, with H_2 elimination, are considered, as the following:



where $m = 1$ or 2 . The rate parameters are estimated from analogous dissociation reactions.¹⁵

The rate coefficient for electron detachment (ed) from anionic clusters (reaction type 6) increases with the cluster size, and the upper limits are given by²⁰

$$k_{\text{ed,max}} \approx 1.7 \times 10^{-8} T_e^{1/2} m^{2/3} \text{ (cm}^3 \text{ s}^{-1}\text{)}, \quad (13)$$

where m is the number of molecular units in m -mers.

The last two types of electron-impact reactions are electron recombination reactions. Dissociative recombination (reaction type 8) is known to be a much faster process in general than nondissociative (radiative) recombination (reaction type 7). The rate constants are weakly dependent on the properties of ions, and have typical values of^{1,22}

$$k_{dr} \approx \frac{1 \times 10^{-7}}{\sqrt{T_e \text{ (eV)}}} \text{ (cm}^3 \text{ s}^{-1}\text{)}, \quad (14)$$

$$k_{rr} \approx \frac{1 \times 10^{-13}}{\sqrt{T_e \text{ (eV)}}} \text{ (cm}^2 \text{ s}^{-1}\text{)}, \quad (15)$$

where k_{dr} and k_{rr} represent dissociative and radiative recombination rate constants, respectively.

An approximate scaling law was proposed by Hickman²³ for the reaction rates for mutual neutralization between anionic and cationic clusters (reaction types 9 and 10):

$$k_{\text{neutral}} \approx 5.34 \times 10^{-7} \text{EA} - 0.4 m_r^{-0.5} (T_i/300)^{-0.5} \text{ (cm}^2 \text{ s}^{-1}\text{)}, \quad (16)$$

where EA is the electron affinity of the parent neutral species of the anion in eV, m_r is the reduced mass in atomic mass

units, and T_i is the ion temperature in K. Neutralization is assumed to occur associatively for silicon oxide clusters larger than the trimer.

Last, clustering between charged and neutral silicon oxide clusters is considered (reaction type 11). The Langevin collision rate is known to represent a theoretical upper limit for ion–molecule collision rates, as given by²⁰

$$k_{\text{Langevin}} \approx 2.34 \times 10^{-9} (\alpha/m_r)^{1/2} \text{ (cm}^2 \text{ s}^{-1}\text{)}, \quad (17)$$

where α is the polarizability of the neutral species in \AA^3 , and m_r is the reduced mass in atomic mass units. Equation (17) shows that the Langevin rate is not strongly dependent on the polarizability. Since the polarizabilities of silicon oxide clusters are not well known, an approximate scaling law for silane molecules²⁰ is used where the polarizability increases with the number of silicon atoms. The contribution from oxygen and hydrogen atoms is ignored:

$$\alpha_{(\text{SiO}_x)_n} \approx \alpha_{\text{SiH}_4} [1 + 0.8(n-1)]. \quad (18)$$

B. Thermochemistry of ionic silicon oxide clusters

As the number of molecular units in a neutral k -mer increases, its electron affinity, EA_k , increases while the ionization potential, IP_k , decreases. Makov *et al.*²⁴ proposed expressions for EA_k and IP_k of dielectric clusters:

$$\text{EA}_k = \text{EA}_\infty - \frac{1}{2} \frac{e^2}{4\pi\epsilon_0(r_k + \delta)} \left(\frac{\epsilon_i - 1}{\epsilon_i} \right), \quad (19)$$

$$\text{IP}_k = \text{IP}_\infty + \frac{1}{2} \frac{e^2}{4\pi\epsilon_0(r_k + \delta)} \left(\frac{\epsilon_i - 1}{\epsilon_i} \right), \quad (20)$$

where EA_∞ and IP_∞ are, respectively, the electron affinity and ionization potential of a flat surface, and e , ϵ_i , ϵ_0 , r_k , and δ are, respectively, the elementary charge, relative permittivity (i.e., the absolute permittivity divided by the permittivity of free space), permittivity of free space, cluster radius, and a radius correction. EA_∞ and IP_∞ can be estimated from the known properties of SiO and SiO_2 monomers.^{25,26} To first approximation we assume $\delta = 0$, $\epsilon_i = 5.8$ for SiO clusters, and $\epsilon_i = 4.4$ for SiO_2 clusters.^{21,26} The resulting values for SiO and SiO_2 clusters, together with the estimated radii based on their ground state molecular structures,²⁵ are summarized in Table II.

The heats of formation of charged clusters are obtained from the values of the corresponding neutral clusters by assuming that they differ by their ionization potentials or electron affinities depending on their charge status given by Eqs. (21) and (22), whereas specific heats and entropies are assumed to be the same for ions as for their parent neutrals.

$$\Delta H_{f,l}^0[(\text{SiO}_x)_n^-] = \Delta H_{f,l}^0[(\text{SiO}_x)_n] - \text{EA}_n, \quad (21)$$

$$\Delta H_{f,l}^0[(\text{SiO}_x)_n^+] = \Delta H_{f,l}^0[(\text{SiO}_x)_n] + \text{IP}_n. \quad (22)$$

The thermochemical properties of charged silicon oxide clusters are expressed in terms of polynomial fitting coefficients in the standard NASA format used in the CHEMKNIN family of codes.²⁷ The fitting coefficients are presented in the Appendix.

TABLE II. Estimates of the electron affinities and ionization potentials of silicon oxide clusters.

K	SiO clusters			SiO ₂ clusters		
	r_k^a (Å)	EA _k (eV)	IP _k (eV)	r_k^b (Å)	EA _k (eV)	IP _k (eV)
1	4.10	0.22	11.43	4.86	2.21	12.13
2	4.52	0.37	11.28	9.37	2.85	11.49
3	4.99	0.50	11.15	12.26	3.02	11.32
4	5.66	0.66	10.99	15.14	3.12	11.22
5	6.08	0.73	10.92	18.03	3.18	11.16
6	6.63	0.82	10.83	20.92	3.23	11.11
7	7.18	0.90	10.75	23.80	3.27	11.07
8	7.73	0.96	10.69	26.69	3.30	11.04
9	8.28	1.02	10.63	29.57	3.32	11.02
10	8.83	1.07	10.58	32.46	3.34	10.99
∞	∞	1.8	9.85	∞	3.54	10.80

^a r_k is assumed to be one half of the longest diagonal of the ground state k -mer (Ref. 31).

^b r_k is assumed to be one half of the length of the linear chain of the ground state k -mer (Ref. 31).

C. Surface reaction mechanism

The heterogeneous chemistry at the deposition surface is not precisely modeled in this study. Positively charged species are known to gain a considerable amount of extra energy near the film deposition substrate due to the large gradient of electric potential inside the sheath. The accelerated positive species can produce a synergistic effect on the surface chemistry and thus on film growth and etching processes.²⁸ However, since the computational domain of interest in this study does not include the sheath region, as will be discussed below, a detailed treatment of heterogeneous chemistry that leads to a reliable prediction of film growth is not pursued. Instead, a simplified approach is used. The surface reaction mechanism serves somewhat as a boundary condition for the species mass conservation equations, and a sticking probability is assigned to each gas species arriving at the deposition surface (more precisely speaking, at the sheath edge).

Neutral radicals are assumed to stick with unity probability unless their surface reactivities are known from the literature. Positively charged species are assumed to neutralize at the surface via electron recombination reactions. All other species, including negatively charged clusters, are assumed to be nonreactive and thus to have zero net flux to the surface.

III. 1D PLASMA REACTOR MODEL

A. Overview and assumptions

An ICP reactor is modeled by considering a Gaseous Electronics Conference (GEC) reference cell.²⁹ The flow in the center region of the reactor is assumed to be an axisymmetric stagnation-point flow between two parallel plates, separated by a distance of 6.8 cm. A detailed derivation of the governing equations in this geometry in thermal environments can be found in the work of Coltrin *et al.*³⁰ The governing equations can be reduced to one-dimensional form

through a similarity transformation.³¹ To account for additional dominant features of ICPs, an extended set of conservation equations is formulated for mass, momentum, and energy within a multicomponent two-temperature framework.

Reactant gases are introduced at a given mass flow rate through the inlet showerhead, where the induction coils are assumed to be located (6.8 cm distance from the substrate). A driving frequency of 13.56 MHz for the radio frequency (rf) power is assumed.

The externally induced electromagnetic field is assumed to decay exponentially in the plasma due to the skin effect. While the heating of electrons through the inductive field is included in our model, heavy particles are unaffected due to their inertia. Charged species transport relative to the mixture-averaged velocity is determined by the space-charge-induced electric field, which is obtained by assuming plasma quasineutrality.

Both the inlet showerhead and the substrate are treated as deposition surfaces. A very thin sheath is assumed to exist by imposing a discontinuity in the plasma potential at each boundary, so that the sheath regions can be excluded from the computational domain. This assumption together with quasineutrality enables one to reduce the computational expense by avoiding the need to consider the sharp gradients inside the sheaths and an additional set of equations for the electric fields.

Due in part to the complexity of the model, we avoid the solution of the Boltzmann equation by assuming a Maxwellian electron energy distribution function. This is a reasonable working assumption, especially considering the paucity of fundamental data such as the collision cross sections for electron impact reactions that involve silicon oxides. Since there is experimental evidence for non-Maxwellian behavior of the electron distribution function in ICPs,¹¹ solution of the Boltzmann equation may be added in future studies.

The electron temperature is obtained separately by solving the electron energy equation. All heavy species regardless of their size and charge are assumed to be at a common, specified gas temperature that is uniform over the reactor space, although in general there could be gradients in gas temperature depending on the reactor configuration.

B. Governing equations

The set of governing equations that describe the stagnation-point flow between two infinite parallel plates in a thermal system can be found elsewhere.³⁰ Here in Sec. III B, additional governing equations and source terms are presented that take into account the model assumptions discussed in Sec. III A.

Gas species are transported by convection, diffusion, and, if charged, by the ambipolar potential field. The mass conservation equation of the k th gas species is given by

$$\rho \frac{\partial Y_k}{\partial t} + \rho \mathbf{u} \nabla Y_k = -\nabla \cdot \mathbf{j}_k + W_k, \quad k = 1, 2, \dots, K_g, \quad (23)$$

where ρ , \mathbf{u} , Y_k , W_k , and $\dot{\omega}_k$ are, respectively, mass-averaged mixture density, mass-averaged mixture velocity, mass frac-

tion, molecular weight, and net production rate of the k th species. The k th species mass flux \mathbf{j}_k relative to \mathbf{u} can be expressed as³²

$$\mathbf{j}_k = \rho Y_k \frac{D_{km}}{X_k} \nabla X_k + \rho Y_k \sum_{j \neq e} \frac{Y_j}{X_j} D_{jm} \nabla X_j + \frac{\rho Y_k}{k_B T} \left(q_k e D_{km} - \sum_{j \neq e} q_j e Y_j D_{jm} \right) \mathbf{E}_{\text{ambi}}, \quad k \neq e, \quad (24)$$

$$\mathbf{j}_e = - \frac{m_e}{q_e} \sum_{k \neq e} \frac{q_k}{m_k} \mathbf{j}_k, \quad (25)$$

where k_B , T , e , X_k , D_{km} , m_k , and q_k are, respectively, the Boltzmann constant, gas temperature, elementary charge, mole fraction, mixture-averaged diffusion coefficient, the molecular mass, and the number of charges per molecule of the k th species.

The electron mass flux is determined from ambipolarity by Eq. (25), where the subscript e denotes electron. The ambipolar electric field, \mathbf{E}_{ambi} , is related to the electron concentration gradient, and is given by

$$\mathbf{E}_{\text{ambi}} = \frac{k_B T_e \nabla X_e}{q_e e X_e}. \quad (26)$$

The plasma potential can be computed by integrating Eq. (26). The electron number density, n_e , can be calculated either by considering species mass continuity, Eq. (23), or by plasma quasineutrality, $n_e = \sum_{k=\text{cations}} n_k - \sum_{k=\text{anions}} n_k$.

The electron energy equation takes the following form:^{33,34}

$$\frac{\partial(\rho_e i_e)}{\partial t} + \nabla \cdot (\rho_e i_e \mathbf{u}) + p_e \nabla \cdot \mathbf{u} - \mathbf{j}_e \cdot \mathbf{F}_e - \dot{\omega}_e W_e \Delta \tilde{h}_e = - \nabla \cdot \mathbf{Q}_e'' - \dot{Q}_{\text{loss}}^{\text{elas}} - \dot{Q}_{\text{loss}}^{\text{inelas}} + \dot{Q}_{\text{gain}}^{\text{inductive}}, \quad (27)$$

where p_e , ρ_e , and i_e are, respectively, the partial pressure, mass density, and internal energy of electrons. The internal energy per unit mass of electrons can alternatively be expressed as $i_e = 3k_B T_e / 2m_e$ or $i_e = h_e - k_B T_e / m_e$, where h_e is the specific enthalpy of electrons. The second and third terms on the left-hand side (lhs) of Eq. (27) take into account the contributions of convective and pressure forces, respectively. The fourth term accounts for a body force produced by the ambipolar electric field $\mathbf{F}_e = q_e e \mathbf{E}_{\text{ambi}} / m_e$. The thermalization of newly formed electrons with other electrons is considered in the last term on the lhs, with the electron enthalpy given by $\Delta \tilde{h}_e = -5k_B T_e / 2m_e$.

The first term on the right-hand side (rhs) of Eq. (27) accounts for the conductive heat flux of electrons, and can be expressed as

$$\mathbf{Q}_e'' = - \frac{5}{2} n_e k_B D_e \nabla T_e + \frac{5}{2} \frac{k_B T_e}{m_e} \mathbf{j}_e. \quad (28)$$

Here D_e is the electron diffusion coefficient, given by

$$D_e = \mu_e \frac{k_B T_e}{e} = \frac{k_B T_e}{m_e \nu_{en}}, \quad (29)$$

where μ_e is the electron mobility and ν_{en} is the total momentum transfer collision frequency of an electron with neutrals, which can be expressed as $\nu_{en} = \sum_{k=\text{neutral}} \nu_{ek}$.

Energy transfers by elastic and inelastic collisions are included in the next two terms on the rhs of Eq. (27), and can be expressed as

$$\dot{Q}_{\text{loss}}^{\text{elas}} = 3k_B n_e (T_e - T) \sum_{k=1}^{kg} \frac{W_e}{W_k} \nu_{ek}, \quad k \neq e, \quad (30)$$

$$\dot{Q}_{\text{loss}}^{\text{inelas}} = \sum_{r=1}^{Iei} \Delta H_r A_r, \quad (31)$$

where I_{ei} , ΔH_r , and A_r are, respectively, the total number of electron-impact reactions, the net enthalpy change of the r th reaction, and the net rate of progress of the reaction.

Inductive heating of electrons by the external electric field is given by the last term on the rhs of Eq. (27). The power deposition per unit volume of the gas mixture can be expressed as

$$\dot{Q}_{\text{gain}}^{\text{inductive}} = \frac{1}{2} \text{Re}(\sigma_p |\mathbf{E}_{\text{ind}}|^2). \quad (32)$$

The plasma conductivity can be obtained from $\sigma_p = \epsilon_0 \omega_{pe}^2 / \nu_{en} - i\omega$,³⁵ where ϵ_0 is the permittivity of free space. The plasma frequency is determined from $\omega_{pe} = (e^2 n_e / m_e \epsilon_0)^{1/2}$. The angular frequency $\omega = 2\pi f$, where f is the antenna frequency of the induction coils, is assumed to equal 13.56 MHz. The external electric field induced by the induction coils, \mathbf{E}_{ind} , can be expressed by the standard skin effect law³⁵ as

$$\mathbf{E}_{\text{ind}} = -E_0 \exp\left(-\frac{|z|}{\delta}\right), \quad (33)$$

where the skin depth can be expressed as $\delta = (\omega/c \text{Im} \epsilon_p^{1/2})^{-1}$. Here c is the speed of light, and the relative plasma permittivity is given by $\epsilon_p = 1 - [\omega_{pe}^2 / \omega(\omega - i\nu_{en})]$.

C. Boundary conditions

The flux of negative ions is set to zero at the boundaries, whereas the mass fluxes of neutrals and of positive ions are balanced by their surface production rates, given by

$$\mathbf{j}_k = \dot{s}_k W_k + \rho \mathbf{u}_\infty Y_{k,\infty}, \quad \text{at } z=0, \quad (34)$$

$$\mathbf{j}_k = \dot{s}_k W_k, \quad \text{at } z=L, \quad (35)$$

where \dot{s}_k , \mathbf{u}_∞ , and $Y_{k,\infty}$ are the surface production rate, inlet velocity, and inlet mass fraction of the k th species, respectively. Radicals and neutral clusters are assumed to react with unity probability at both boundaries.

To convert the sticking probability expression of the surface recombination reactions that involve positive ions to the usual kinetic rate constants, the following relation³⁶ is used:

$$k_{\text{Bohm}} = \frac{\gamma_i}{(\Gamma)^m} \sqrt{\frac{k_B T_e}{W_{\text{ion}}}}, \quad (36)$$

where γ_i is the sticking (reaction) probability of the i th reaction, Γ is the surface site density, and m is the sum of the stoichiometric coefficients of reactants in the i th reaction that

are surface species. This expression uses the assumption that the ions enter the sheath with the Bohm velocity, $\sqrt{k_B T_e / W_{\text{ion}}}$.

IV. NUMERICAL IMPLEMENTATION: A MODIFICATION OF SPIN

SPIN,³⁷ the CHEMKIN²⁷ application program for one-dimensional stagnation-flow CVD reactors, was modified to solve the stagnation-point flow. The set of governing equations including Eqs. (23) and (27) must be solved simultaneously together with the silane-oxygen-argon plasma chemistry and the chemical clustering mechanism.

Although time-dependent simulations were conducted in this study to reduce computational difficulties, a steady-state solution was ultimately intended. The simulation results were obtained after a time integration of a few milliseconds, during the latter part of which the solution did not change noticeably. However, it is not clear physically whether a steady-state solution exists in a plasma system, especially one in which particle formation takes place, since negatively charged particles can be trapped in the plasma and undergo a growth process for a long while, thereby affecting the plasma.

TWOPNT,³⁸ a boundary-value-problem solver based on the modified Newton method, was used to search iteratively for converged solutions. Time-dependent calculations were performed here. Initially the species concentrations everywhere in the reactor space were set to be the same as the inlet condition. However, for the range of conditions considered in this study, the solution became practically independent of the initial conditions after a few tens of microseconds of time integration. The time step had to be maintained at less than 10^{-8} s to guarantee convergence. For a time integration of 3 ms, a typical run required about 20 CPU hours on an SGI Origin 2000 supercomputer.

V. SIMULATION RESULTS

In order to validate our model, we performed initial simulations for a pure oxygen plasma. Results of the simulations are compared with experimental and modeling results of Gudmundsson and Lieberman³⁹ in Figs. 1 and 2. Figure 1 shows the electron density as a function of rf power. The predictions of our model agree to within about 50% with the predictions of the Gudmundsson and Lieberman model. Also, the comparison with their measured electron densities is good. Electron temperatures as a function of the rf power applied are shown in Fig. 2. Our model yields electron temperatures that are within 3% of the Gudmundsson and Lieberman model. The measurements of these authors, performed at different pressures, gave higher temperatures than predicted by both models. However, it is well known that Langmuir probe measurements in rf plasma often tend to overestimate the electron temperature. In general, the comparison of our model to the results published by Gudmundsson and Lieberman is very reasonable.

Since our simulation results for an oxygen plasma appear reasonable, we now turn to the more complicated case of a

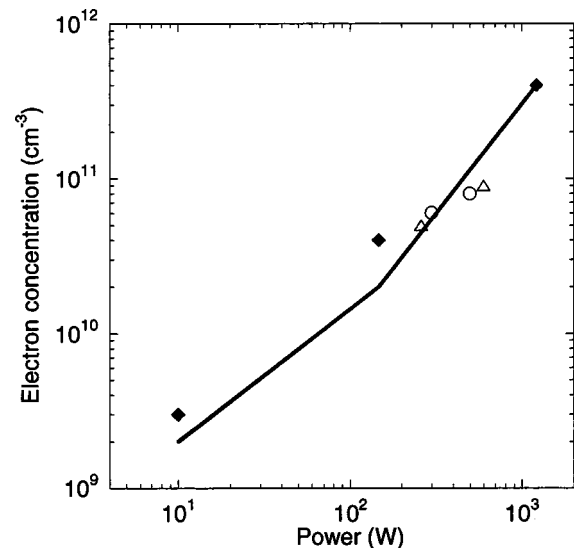


FIG. 1. Electron concentration at reactor midplane vs power for a pure oxygen plasma at 20 mTorr and an oxygen flow rate of 10 sccm. Solid line: Predictions of the present model. Symbols: Model predictions of Gudmundsson and Lieberman (Refs. 39) (◆) and their experimental data at 10 (○) and 60 mTorr (△).

silane-oxygen-argon plasma. The flow rates of argon, oxygen, and silane are, respectively, 100, 2.3, and 1.0 sccm. We first consider a base case in which the pressure is fixed at 100 mTorr, the power input at the induction coil is equal to 1.9 W cm^{-2} , and the gas heavy species temperature is fixed at 500 K.

For the base case conditions, Fig. 3 shows the predicted species concentration profiles for all nonsilicon-containing species present anywhere in the domain at a concentration above 10^{10} cm^{-3} . The shapes of these profiles are primarily affected by two factors: (1) the deposition of power into the plasma close to the induction coil that is located 6.8 cm from the substrate; and (2) whether or not a given species is assumed to be reactive at surfaces.

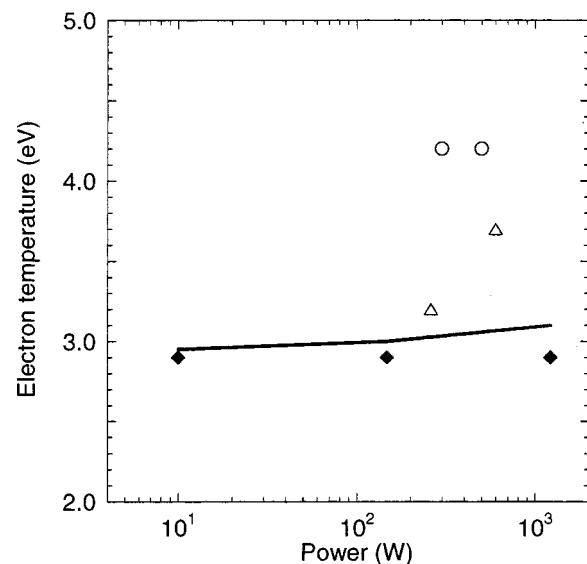


FIG. 2. Electron temperature at the reactor midplane, with the same conditions and comparisons as those in Fig. 1.

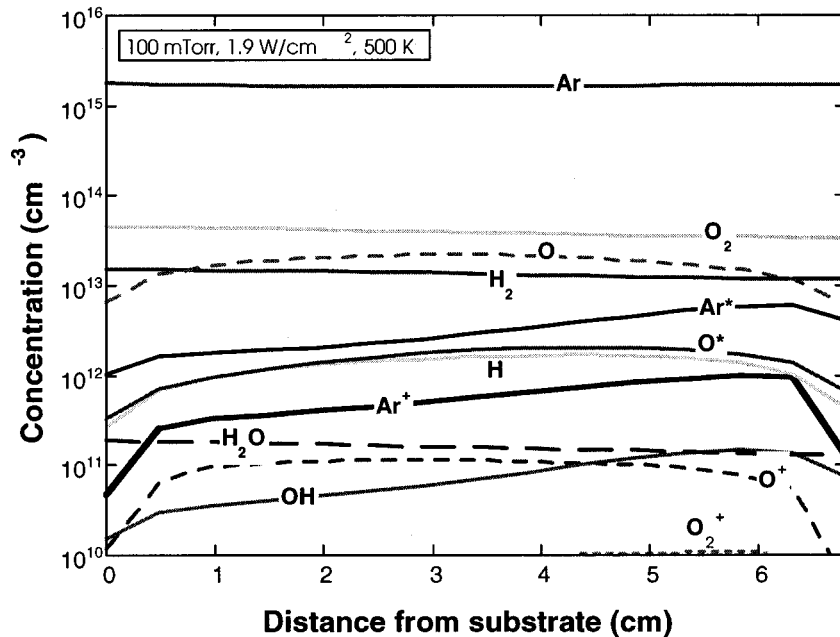


FIG. 3. Predicted concentration profiles of dominant nonsilicon-containing species for base case conditions: pressure=100 mTorr, power density=1.9 W cm⁻², gas temperature=500 K.

The first factor causes the concentration profiles of excited-state argon (Ar^*), argon ions, and OH to peak close to the induction coil (however, see also the discussion accompanying Fig. 9 below). The second factor causes the concentration profiles of radical species such as O and H to drop close to the surfaces, whereas the profiles of O_2 , H_2 , and Ar are relatively flat.

Figure 4 shows the predicted base case concentration profiles of the dominant species that contain one or two silicon atoms. Silane decomposition is seen to be over 90% complete by the middle of the axial domain. The SiO dimer is predicted to be the most abundant species, followed by the SiO monomer and then the SiO_2 dimer. The next most abundant silicon oxide species are predicted to be SiH_2O and the

HSiOOH dimer. As discussed in Sec. III A, these species are believed to be potentially important in silicon oxide clustering, through hydrogen elimination reactions (3) and (4).

Figure 4 also indicates that the concentration of silicon dimers, Si_2 , rises steeply toward the deposition substrate, finally becoming the most abundant silicon-containing species at $x=0$. However we believe that the predicted abundance of Si_2 is an artifact of the model's limitations. Si_2 is one of the end products of chain terminating reactions in silane oxidation. Our mechanism does not consider its destruction in subsequent reactions, nor is it assumed to react at surfaces. Therefore its predicted concentration is expected to be artificially high. We do not expect bare silicon clustering

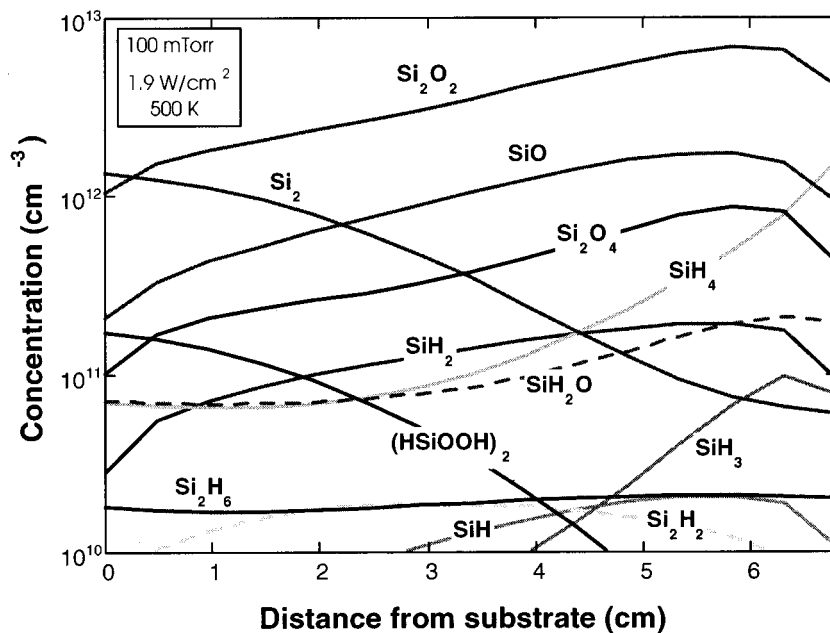


FIG. 4. Predicted concentration profiles of dominant species containing one or two silicon atoms for base case conditions.

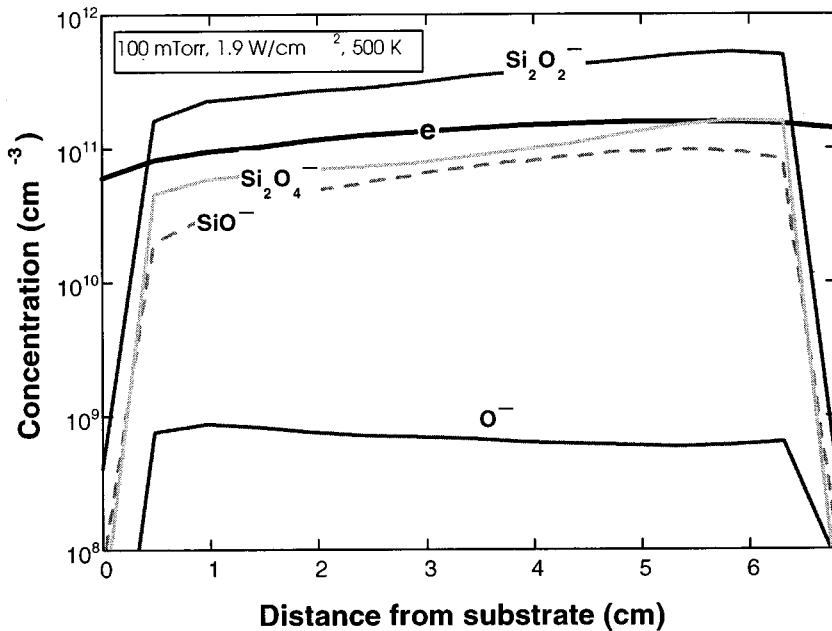


FIG. 5. Predicted concentration profiles of dominant negatively charged species for base case conditions.

to be significant in this system, because of the high relative abundance of oxygen and hydrogen.

Figure 5 shows the concentration profiles of the dominant negatively charged species, exclusive of species containing more than two silicon atoms. These profiles all drop sharply near the electrodes, because anions are electrostatically confined in the plasma, except for the electrons, which are at much higher temperature (see also the discussion accompanying Fig. 10 below). The electron concentration is predicted to equal $\sim 10^{11} \text{ cm}^{-3}$, but it is interesting to note that the dominant negatively charged species over most of the plasma are not electrons but the SiO dimer anion, which is formed by electron attachment to the abundant neutral SiO dimer.

Figure 6 shows the predicted concentration profiles for

neutral SiO clusters. Consistent with Fig. 4, the SiO dimer is predicted to be more abundant than the monomer, but otherwise the relative abundance follows a monotonically decreasing sequence as the cluster size increases. Insofar as the largest clusters included in the simulation can be treated as “particles,” these results suggest a particle concentration in the range of 10^7 – 10^8 cm^{-3} .

For clusters of any given size the base case calculations predict that neutrals are most abundant, followed by anions and then cations. The calculations also predict that SiO clusters are far more abundant than SiO₂ clusters, consistent with the relative abundances seen in Fig. 4. These trends are illustrated in Fig. 7, in this case for trimers.

The primary clustering pathways in the center of the re-

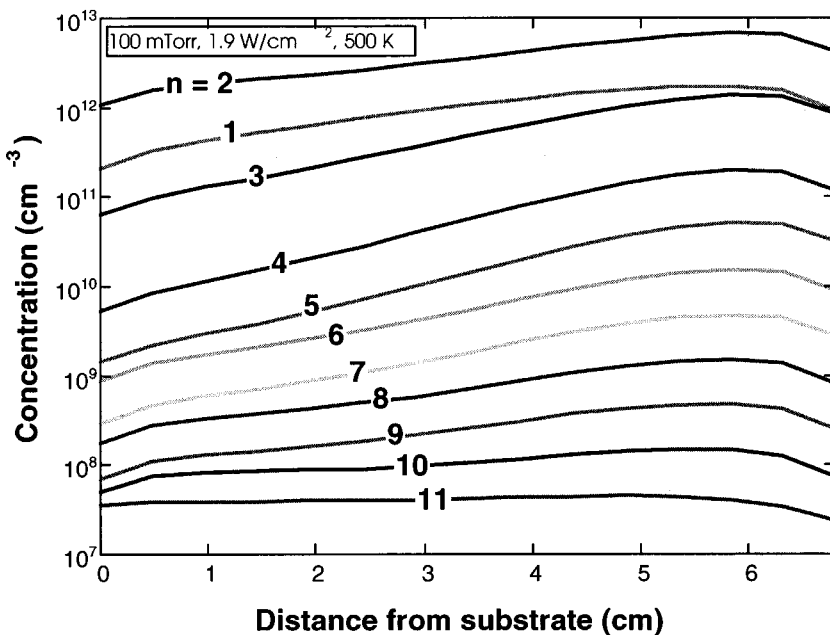


FIG. 6. Predicted concentration profiles of neutral $(\text{SiO})_n$ clusters for base case conditions.

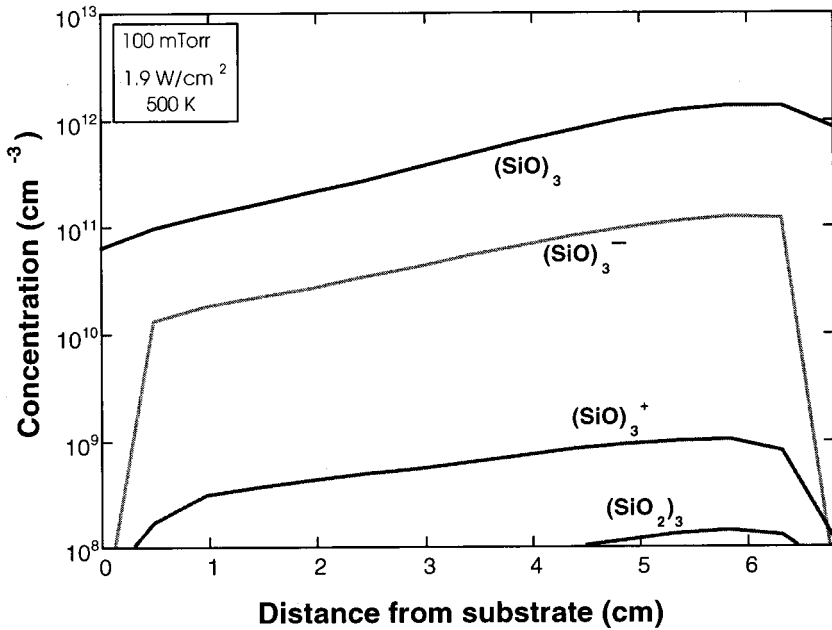


FIG. 7. Predicted concentration profiles of dominant trimer clusters for base case conditions.

actor for the base case conditions are shown in Fig. 8. Positive clusters are predicted to play little role in clustering because of their recombination reactions either at the surfaces or in the gas phase. Anionic monomers and dimers are produced by electron attachment to their neutrals. The anionic clusters grow mainly by the addition of SiO dimers produced by the dissociation of $(\text{SiH}_2\text{O})_2$, because dimers are predicted to be more abundant than monomers. Neutralization of anions is predicted to occur at much faster rates than clustering among neutrals. This explains why the neutral clusters exhibit higher concentrations in Figs. 6 and 7 relative to anionic clusters. Anionic clusters might have been expected to be the major species since the plasma potential confines

them to the reactor center, allowing relatively long residence times if the neutralization rate is not fast enough. The primary clustering pathways are expected to remain largely unaffected by the change in pressure or power, although the magnitude of the rates will change, a result of the variation in precursor concentrations and from pressure-dependent kinetics.

Figures 9–12 explore the effects of varying several process parameters, including pressure, power input, and gas (i.e., heavy species) temperature. In each case the base case results are compared to simulations in which one of the parameters was varied, as indicated in Figs. 9–12, while the other parameters were kept the same as in the base case.

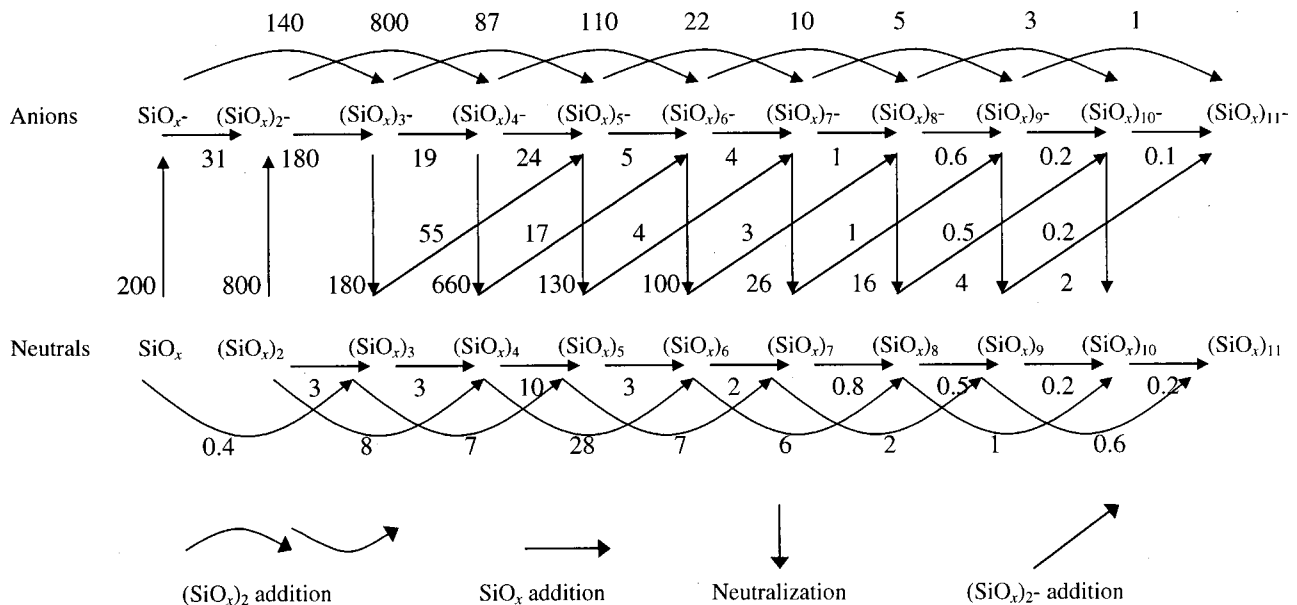


FIG. 8. Primary clustering pathways: base case. Arrows and numbers represent the net direction and the net production rates of the reaction in units of 10^{-12} mol cm^{-3} s^{-1} .

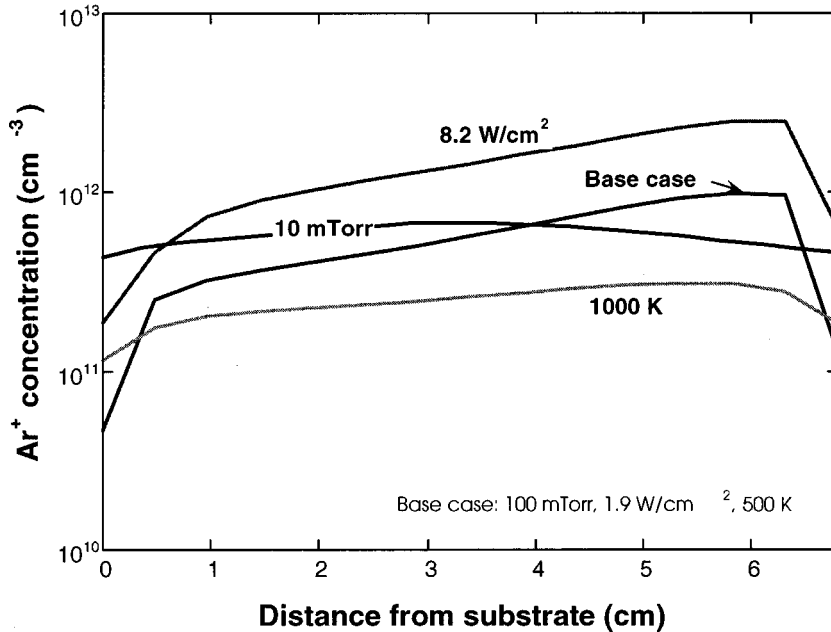


FIG. 9. Predicted argon ion concentration profiles for the base case and for cases in which either the pressure, power, or gas temperature was varied, keeping all other conditions the same as those in the base case.

Figure 9 shows the spatial profiles of the positive ion density for all cases considered. As seen in Fig. 3, the Ar⁺ ions are the dominant ions and the only ones that appear with a concentration greater than 10¹⁰ cm⁻³. The ion density profile of the base case (100 mTorr, 1.9 W cm⁻², 500 K) shows strong asymmetry with a peak close to the position of the induction coil. This is caused by the strongly asymmetric rf electric field that decreases rapidly in the skin layer, and additionally by the fact that at 100 mTorr both the electron and ion transport are strongly collision dominated. The resulting localized energy dissipation of the electrons causes an ionization profile that is peaked close to the induction coil. At higher power (8.2 W cm⁻²) the axial ion density profile has approximately the same shape as in the base case and the

ion density increases in rough proportion to the increase in power. Increasing the gas temperature to (1000 K) or decreasing the pressure to (10 mTorr) both lead to a less collisional electron transport and correspondingly to less localized electron energy dissipation. At 100 mTorr and 1000 K the ion density profile still shows a slight peak close to the induction coil but far less pronounced than at 500 K. At 10 mTorr, the ion density profile becomes almost symmetric with a maximum in the center. While the electrons are still mainly heated in the skin layer close to the induction coil, the low pressure enables efficient energy transport via the electrons throughout the plasma volume (nonlocal case).

Figure 10 shows the corresponding electron density profiles. The electron density profiles are far more uniform and

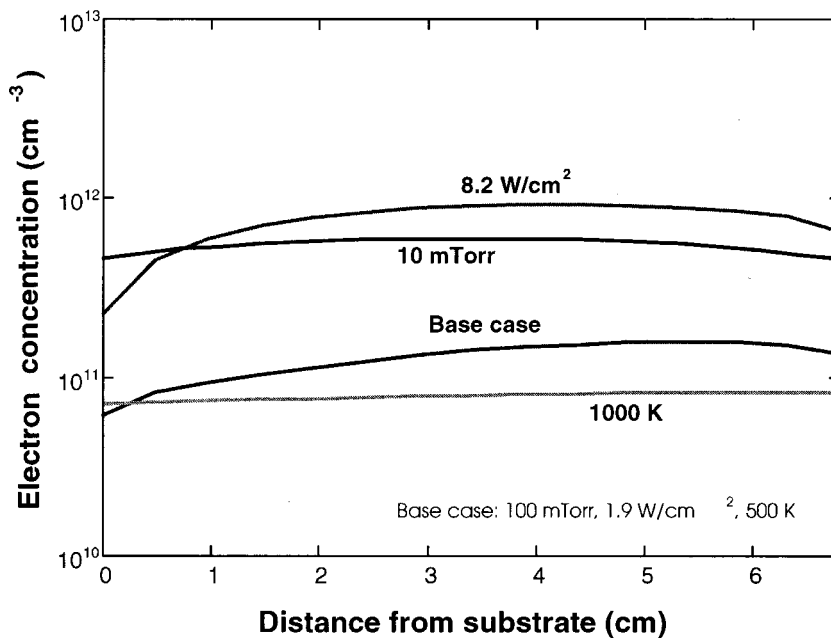


FIG. 10. Predicted electron concentration profiles, with comparisons similar to those in Fig. 9.

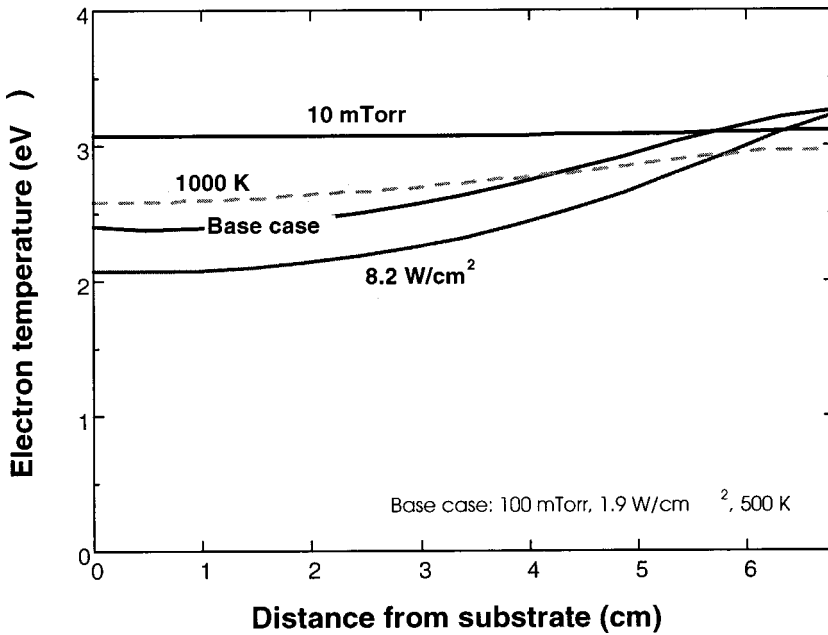


FIG. 11. Predicted profiles of electron temperature, with comparisons similar to those in Fig. 9.

symmetric than the positive ion profiles due to the fact that the electron temperature is much higher than the heavy species temperature. The ambipolar space charge potential hence adjusts such that the negative ion profile more closely resembles the positive ion profile seen in Fig. 9. The relatively small potential variations needed to achieve this cause the electron density profile to lack the peaks seen in the positive ion profiles. In the 10 mTorr case, the electron and positive ion density are almost equal. This is a result of the negligible clustering predicted in this case (see below), and negative ions are insignificant. For the 100 mTorr cases, the increase of rf power from 1.9 to 8.2 W/cm² leads to a relatively stronger increase in the electron density than was observed in the positive ion density in Fig. 9. This means that with an

increase in rf power the plasma becomes less electronegative. Increasing the gas temperature at constant pressure leads to a drop of the electron density compared to the base case. This may simply be related to the associated decrease in the neutral gas density as the temperature increases at fixed pressure. However, the drop in electron density is less pronounced than observed for the positive ion density, which means that at higher gas temperature the plasma again becomes more electronegative. All these trends are consistent with the well-known behavior of simple electronegative gases, i.e., that the electronegativity of the plasma $\alpha = n_n/n_e$ scales with the ratio of electron density to neutral gas density as $(n_e/n_g)^{-1/2}$, with n_n the negative ion density and n_g the neutral gas density.⁴⁰

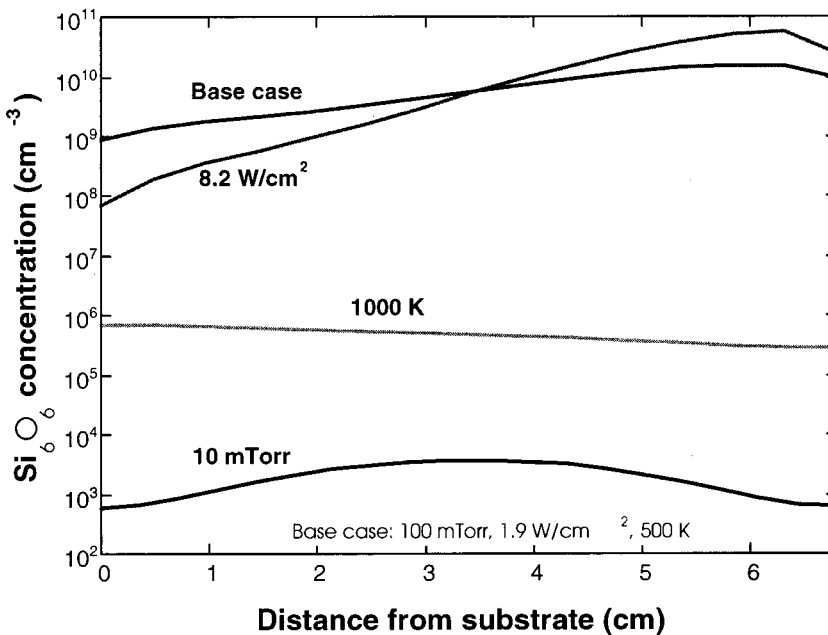


FIG. 12. Predicted concentration profiles of (SiO)₆, with comparisons similar to those in Fig. 9.

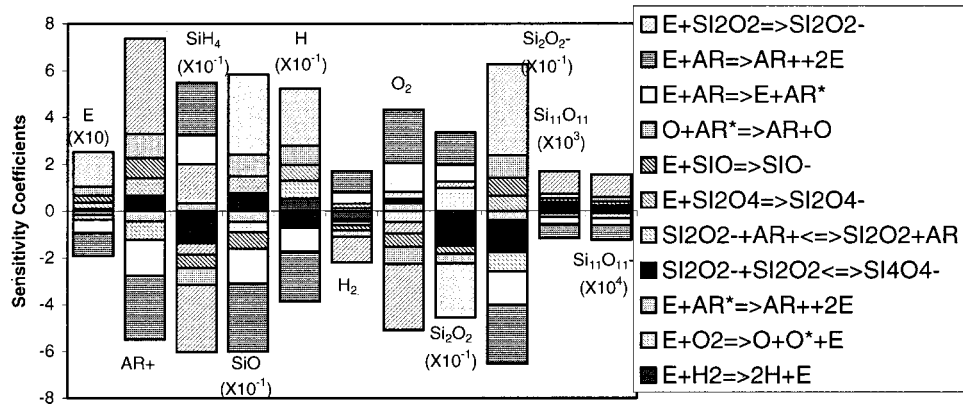


FIG. 13. Normalized sensitivity coefficients for the base case at the reactor midplane. Absolute values of the coefficients can be obtained by multiplying by the numbers in parentheses.

Figure 11 shows the predicted axial electron temperature profiles. The flat temperature profile at 10 mTorr demonstrates that at this low pressure the energy transport through the electrons is very efficiency and the temperature profile is decoupled from the nonuniform profile of rf heating in the skin layer. In the higher pressure cases, the rf power dissipation becomes more localized through decreased electron energy transport, leading to a maximum of the electron temperature close to the induction coil. This effect is more pronounced at the low gas temperature of 500 K than at 1000 K due to the higher neutral gas density at the lower temperature. As expected, the average electron temperature at 10 mTorr is higher than at 100 mTorr in order for ionization to balance the larger particle loss rates at lower pressures.

Figure 12 shows the concentration profiles of the hexamer. First of all, pressure is shown to have the most significant effect in clustering, with the concentration dropping six orders of magnitude when pressure is reduced from 100 to 10 mTorr. Also shown is the considerable effect of the gas temperature. In the case where the gas temperature is doubled to 1000 K, the hexamer concentration is shown to drop three orders of magnitude, below 10^6 cm^{-3} . This is due to the increased rates of dissociation of silicon oxide clusters at elevated temperature. In reaction types 11 and 12 in Table I, the reverse directions become increasingly favored at higher temperatures, and clustering cannot proceed as fast beyond the first few steps. Compared to the base case at 500 K, the production rates of anionic dimers and trimers decrease by more than two orders of magnitude at 1000 K. For the higher power case, 8.2 W/cm^2 , the increased electron concentration (see Fig. 10) and the more localized electron temperature profile (larger gradient near the inlet; see Fig. 11) cause the peak concentration to increase and to shift toward the induction coil.

A sensitivity analysis was performed to assess the predominant reactions that contribute to species concentration profiles. We adopted the approach of Coltrin *et al.*,³⁷ which utilizes Jacobian and LU factorization that are already available from the original solution algorithm, using the modified Newton method. Figure 13 shows the normalized sensitivity coefficients of several species of interest in the center of the reactor for the base case conditions. The computed sensitivity coefficients, i.e., the rates of change of solution variables

with respect to system parameters, can be expressed in the following form:

$$\frac{\alpha_i}{X_k} \frac{\partial X_k}{\partial \alpha_i} = \frac{\alpha_i}{Y_k} \frac{\partial Y_k}{\partial \alpha_i} - \alpha_i \bar{W} \sum_j^{K_s} \frac{1}{W_j} \frac{\partial Y_k}{\partial \alpha_i}, \quad (37)$$

where α_i is the pre-exponential factor in the rate constant of the i th reaction. Y_k , X_k , and \bar{W} are, respectively, the mass and the mole fraction of the k th species, and the mean molecular weight of the gas mixture. Among the clustering reactions in Table I, the highest sensitivities for most species are found to be associated with the rate parameters for electron attachment reactions, whose key role is suggested in Fig. 8. The rate constants of electron attachment reactions (reaction type 1) were roughly estimated based on the species-independent maximum cross sections.^{19,20} Other reactions to which the results are highly sensitive include neutralization of a dimer (reaction type 9) and ion-neutral clustering (reaction type 11), for which the rate parameters are again estimated to no better than order-of-magnitude uncertainty.

VI. SUMMARY

A detailed silicon oxide clustering mechanism in low-pressure silane-oxygen-argon plasmas was developed. An inductively coupled plasma reactor was modeled by constructing a set of one-dimensional conservation equations for mass, momentum, and energy within a multicomponent two-temperature framework. Time-dependent simulations were conducted to predict spatial profiles of species concentrations and discharge properties for conditions typical of inductively coupled $\text{SiH}_4\text{-O}_2\text{-Ar}$ high-density plasma. The primary pathways and major contributing processes to clustering were identified. Neutral clusters, produced primarily from neutralization of anionic clusters, were predicted to be more abundant than their charged relatives. Pressure and gas temperature are predicted to have important effects on clustering. A sensitivity analysis identified several reactions that play a key role in the predicted results.

ACKNOWLEDGMENTS

This work was partially supported by NSF GOALI Grant No. CTS-9909563 and by the Minnesota Supercomputing Institute.

APPENDIX: ESTIMATES OF CLUSTER THERMOCHEMICAL PROPERTIES (SEE TABLE III)

TABLE III. Polynomial fitting coefficients for clusters in standard NASA format. The specific heat capacity at constant pressure, C_p^0 , the standard-state enthalpy, H^0 , and the standard-state entropy, S^0 , are, respectively, defined as follows: $C_p^0/\mathfrak{R} = a_1 + a_2T + a_3T^2 + a_4T^3 + a_5T^4$, $H^0/\mathfrak{R}T = a_1 + (a_2/2)T + (a_3/3)T^2 + (a_4/4)T^3 + (a_5/5)T^4 + (a_6/T)$, and $S^0/\mathfrak{R} = a_1 \ln T + a_2T + (a_3/2)T^2 + (a_4/3)T^3 + (a_5/4)T^4 + a_7$, where \mathfrak{R} is the universal gas constant and T is the gas temperature in K. These coefficients are valid only for the gas temperature range of 300–1500 K.

Species	a_1	a_2	a_3	a_4	a_5	a_6	a_7
(SiO) ⁻	3.709 1712E+00	9.069 7284E-04	-4.233 0473E-07	9.034 407E-11	-7.280 2576E-15	-1.064 5630E+04	3.184 2188E+00
(Si ₂ O ₂) ⁻	9.762 5847E+00	-1.593 5308E-04	2.318 0722E-07	-7.572 0988E-11	7.771 6860E-15	-5.765 8950E+04	-2.302 1760E+01
(Si ₃ O ₃) ⁻	1.561 3486E+01	-2.211 6911E-04	3.452 3671E-07	-1.139 6278E-10	1.174 1059E-14	-1.008 6780E+05	-4.974 6628E+01
(Si ₄ O ₄) ⁻	2.115 7012E+01	2.073 9416E-04	1.799 4268E-07	-8.450 1387E-11	9.740 7392E-15	-1.359 6608E+05	-7.056 0939E+01
(Si ₅ O ₅) ⁻	2.619 1211E+01	1.333 8465E-03	-3.272 7956E-07	1.749 2749E-11	2.154 3416E-15	-1.769 8295E+05	-8.829 9259E+01
(Si ₆ O ₆) ⁻	3.185 1958E+01	1.502 8756E-03	-3.012 5048E-07	-1.051 5966E-11	6.134 5351E-15	-2.164 7557E+05	-1.097 0323E+02
(Si ₇ O ₇) ⁻	3.751 2704E+01	1.671 9046E-03	-2.742 2140E-07	-3.852 4681E-11	1.011 4729E-14	-2.558 5748E+05	-1.311 0721E+02
(Si ₈ O ₈) ⁻	4.317 3451E+01	1.840 9336E-03	-2.471 9233E-07	-6.653 3396E-11	1.409 4922E-14	-2.949 9278E+05	-1.525 1118E+02
(Si ₉ O ₉) ⁻	4.883 4197E+01	2.009 9626E-03	-2.201 6325E-07	-9.454 2112E-11	1.807 5115E-14	-3.341 5828E+05	-1.739 1515E+02
(Si ₁₀ O ₁₀) ⁻	5.449 4944E+01	2.178 9916E-03	-1.931 3418E-07	-1.225 5083E-10	2.205 5309E-14	-3.731 9293E+05	-1.953 1913E+02
(SiO ₂) ⁻	6.209 0534E+00	1.363 1043E-03	-5.942 2051E-07	1.199 1553E-10	-9.228 2308E-15	-6.116 5304E+04	-8.428 7447E+00
(Si ₂ O ₄) ⁻	1.412 4110E+01	1.595 0164E-03	-5.422 0059E-07	8.203 3840E-11	-4.467 7341E-15	-1.483 6918E+05	-4.543 5969E+01
(Si ₃ O ₆) ⁻	2.245 9020E+01	1.917 3620E-03	-5.322 1537E-07	5.317 4897E-11	-4.433 4868E-16	-2.355 5923E+05	-8.854 1520E+01
(Si ₄ O ₈) ⁻	3.078 9209E+01	2.250 4993E-03	-5.288 5450E-07	2.594 2087E-11	3.439 3352E-15	-3.213 0783E+05	-1.293 2230E+02
(Si ₅ O ₁₀) ⁻	3.911 1755E+01	2.592 8812E-03	-5.302 7648E-07	-1.378 3655E-13	7.217 4148E-15	-4.067 0226E+05	-1.709 5038E+02
(Si ₆ O ₁₂) ⁻	4.738 5779E+01	3.015 7212E-03	-5.799 7804E-07	-1.383 0300E-11	9.844 7246E-15	-4.918 5220E+05	-2.122 4988E+02
(Si ₇ O ₁₄) ⁻	3.796 7736E+01	3.322 2336E-02	-1.876 2707E-05	4.700 9253E-09	-4.329 1249E-13	-5.675 1238E+05	-1.532 0877E+02
(Si ₈ O ₁₆) ⁻	3.753 4746E+01	4.833 1588E-02	-2.777 2963E-05	7.028 6348E-09	-6.512 3769E-13	-6.479 1765E+05	-1.451 4804E+02
(Si ₉ O ₁₈) ⁻	3.710 1755E+01	6.344 0840E-02	-3.678.3218E-05	9.356 3443E-09	-8.695 6276E-13	-7.282 0717E+05	-1.370 8732E+02
(Si ₁₀ O ₂₀) ⁻	3.666 8764E+01	7.855 0092E-02	-4.579 3473E-05	1.168 4054E-08	1.087 8879E-12	-8.084 9669E+05	-1.290 2659E+02
(SiO) ⁺	3.709 1712E+00	9.069 7284E-04	-4.233 0473E-07	9.034 4073E-11	-7.280 2576E-15	1.189 7702E+05	3.184 2188E+00
(Si ₂ O ₂) ⁺	9.762 5847E+00	-1.593 5308E-04	2.319 0722E-07	-7.572 0988E-11	7.771 6860E-15	7.735 8664E+04	-2.302 1760E+01
(Si ₃ O ₃) ⁺	1.561 3486E+01	-2.211 6911E-04	3.452 3671E-07	-1.139 6278E-10	1.174 1059E-14	3.414 9816E+04	-4.974 6628E+01
(Si ₄ O ₄) ⁺	2.115 7012E+01	2.073 9416E-04	1.799 4268E-07	-8.450 1387E-11	9.740 7392E-15	-9.434 2791E+02	-7.056 0939E+01
(Si ₅ O ₅) ⁺	2.619 1211E+01	1.333 8465E-03	-3.282 7956E-07	1.749 2749E-11	2.154 3416E-15	-4.196 0300E+04	-8.829 9259E+01
(Si ₆ O ₆) ⁺	3.185 1958E+01	1.502 8756E-03	-3.012 5048E-07	-1.051 5966E-11	6.134 5351E-15	-8.145 7958E+04	-1.097 0323E+02
(Si ₇ O ₇) ⁺	3.751 2704E+01	1.671 9046E-03	-2.742 2140E-07	-3.852 4681E-11	1.011 4729E-14	-1.208 3986E+05	-1.311 0721E+02
(Si ₈ O ₈) ⁺	4.317 3451E+01	1.840 9336E-03	-2.471 9233E-07	-6.653 2296E-11	1.409 4922E-14	-1.599 7013E+05	-1.525 1118E+02
(Si ₉ O ₉) ⁺	4.883 4197E+01	2.009 9626E-03	-2.201 6325E-07	-9.454 2112E-11	1.807 5115E-14	-1.991 3563E+05	-1.739 1515E+02
(Si ₁₀ O ₁₀) ⁺	5.449 4944E+01	2.178 9916E-03	-1.931 3418E-07	-1.225 5083E-10	2.205 5309E-14	-2.381 7028E+05	-1.953 1913E+02
(SiO ₂) ⁺	6.209 0534E+00	1.363 1043E-03	-5.942 2051E-07	1.199 1553E-10	-9.228 2308E-15	1.050 2997E+05	-8.428 7447E+00
(Si ₂ O ₄) ⁺	1.412 4110E+01	1.595 0164E-03	-5.422 0059E-07	8.203 2840E-11	-4.467 7341E-15	1.782 6089E+04	-4.543 5969E+01
(Si ₃ O ₆) ⁺	2.245 9020E+01	1.917 3620E-03	-5.322 1537E-07	5.317 4897E-11	-4.433 4868E-16	-6.936 3959E+04	-8.854 1520E+0.1
(Si ₄ O ₈) ⁺	3.078 9209E+01	2.250 4993E-03	-5.288 5450E-07	2.594 2087E-11	3.439 3352E-15	-1.551 1256E+05	-1.293 2230E+02
(Si ₅ O ₁₀) ⁺	3.911 1755E+01	2.592 8812E-03	-5.302 7648E-07	-1.378 3655E-13	7.217 4148E-15	-2.410 8575E+05	-1.709 5038E+02
(Si ₆ O ₁₂) ⁺	4.738 5779E+01	3.015 7212E-03	-5.799 7804E-07	-1.383 0300E-11	9.844 7246E-15	-3.256 5693E+05	-2.122 4988E+02
(Si ₇ O ₁₄) ⁺	3.796 7736E+01	3.322 2336E-02	-1.876 2707E-05	4.700 9253E-09	-4.329 1249E-13	-4.013 1208E+05	-1.532 0877E+02
(Si ₈ O ₁₆) ⁺	3.753 4746E+01	4.833 1588E-02	-2.777 2963E-05	7.028 6348E-09	-6.512 3762E-13	-4.817 2238E+05	-1.451 4804E+02
(Si ₉ O ₁₈) ⁺	3.710 1755E+01	6.344 0840E-02	-3.678 3218E-05	9.356 3443E-09	-8.695 6276E-13	-5.60 0687E+05	-1.370 8732E+02
(Si ₁₀ O ₂₀) ⁺	3.666 8764E+01	7.855 0092E-02	-4.579 3473E-05	1.168 4054E-08	-1.087 8879E-12	-6.424 1717E+05	-1.290 2659E+02

- ¹J. Perrin, C. Böhm, E. Roxana, and A. Lloret, *Plasma Sources Sci. Technol.* **3**, 252 (1994).
- ²C. Hollenstein, A. A. Howling, C. Courteille, D. Magni, S. M. Scholz, G. M. W. Kroesen, N. Simons, W. den Zeeuw, and W. Schwarzenbach, *J. Phys. D* **331**, 74 (1998).
- ³C. R. Gorla, S. Liang, G. S. Tompa, W. E. Mayo, and Y. Lu, *J. Vac. Sci. Technol. A* **15**, 860 (1997).
- ⁴*International Technology Roadmap for Semiconductors* (Semiconductor Industry Association, San Jose, CA, 1999).
- ⁵M. L. Mandich and W. D. Reents, Jr., *J. Chem. Phys.* **96**, 4233 (1992).
- ⁶S. Taylor, J. F. Zhang, and W. Eccleston, *Semicond. Sci. Technol.* **8**, 1426 (1993).
- ⁷B. L. Kickel, J. B. Griffin, and P. B. Armentrout, *Z. Phys. D: At., Mol. Clusters* **24**, 101 (1992).
- ⁸A. J. Lichtenberg, I. G. Kouznetsov, Y. T. Lee, M. A. Lieberman, I. D. Kaganovich, and L. D. Tsedin, *Plasma Sources Sci. Technol.* **8**, 437 (1997).
- ⁹J. D. Bukowski, D. B. Graves, and P. Vitello, *J. Appl. Phys.* **80**, 2614 (1996).
- ¹⁰D. Bose, T. R. Govindan, and M. Meyyappan, *J. Electrochem. Soc.* **146**, 2705 (1999).
- ¹¹U. Kortshagen and B. G. Heil, *IEEE Trans. Plasma Sci.* **27**, 1297 (1999).
- ¹²T. J. Sommerer and M. J. Kushner, *J. Appl. Phys.* **71**, 1654 (1992).
- ¹³M. J. Kushner, W. Z. Collision, M. J. Grapperhaus, J. P. Holland, and M. S. Barnes, *J. Appl. Phys.* **80**, 1337 (1996).
- ¹⁴U. V. Bhandarkar, M. T. Swihart, S. L. Girshick, and U. R. Kortshagen, *J. Phys. D* **33**, 2731 (2000).
- ¹⁵E. Meeks, R. S. Larson, P. Ho, C. Apblett, S. M. Han, E. Edelberg, and E. S. Aydil, *J. Vac. Sci. Technol. A* **16**, 544 (1998).
- ¹⁶E. Meeks, P. Ho, A. Ting, and R. J. Buss, *J. Vac. Sci. Technol. A* **16**, 2227 (1998).
- ¹⁷S.-M. Suh, M. R. Zachariah, and S. L. Girshick, *J. Vac. Sci. Technol. A* **19**, 940 (2001).
- ¹⁸S.-M. Suh, M. R. Zachariah, and S. L. Girshick, *J. Aerosol Sci.* **33**, 943 (2002).
- ¹⁹A. A. Christodoulides, L. G. Christophorou, R. Y. Pal, and C. M. Tung, *J. Chem. Phys.* **70**, 1156 (1979).
- ²⁰J. Perrin, O. Leroy, and M. C. Bordage, *Contrib. Plasma Phys.* **36**, 3 (1996).
- ²¹J. Perrin and C. Hollenstein, *Dusty Plasmas* (Wiley, New York, 1999).
- ²²J. B. A. Mitchell, *Phys. Rep.* **186**, 215 (1990).
- ²³A. P. Hickman, *J. Chem. Phys.* **70**, 4872 (1979).
- ²⁴G. Makov, A. Nitzan, and L. E. Brus, *J. Chem. Phys.* **88**, 5076 (1988).
- ²⁵S. K. Nayak, B. K. Rao, S. N. Khanna, and P. Jena, *J. Chem. Phys.* **109**, 1245 (1998).
- ²⁶*CRC Handbook of Chemistry and Physics*, edited by D. R. Lide (Chemical Rubber, New York, 1996).
- ²⁷R. J. Kee, F. M. Rupley, E. Meeks, and J. A. Miller, Sandia National Laboratories Report No. SAND96-8216, Albuquerque, NM (1996).
- ²⁸J. W. Coburn and H. F. Winters, *J. Appl. Phys.* **50**, 3189 (1979).
- ²⁹P. J. Hargis, Jr. *et al.*, *Rev. Sci. Instrum.* **65**, 140 (1994).
- ³⁰M. E. Coltrin, R. J. Kee, and G. H. Evans, *J. Electrochem. Soc.* **136**, 819 (1989).
- ³¹H. Schlichting, *Boundary-Layer Theory*, 7th ed. (McGraw-Hill, New York, 1979).
- ³²J. D. Ramshaw and C. H. Chang, *Plasma Chem. Plasma Process.* **13**, 489 (1993).
- ³³R. B. Bird, W. E. Stewart, and E. N. Lightfoot, *Transport Phenomena*, 1st ed. (Wiley, New York, 1960).
- ³⁴E. Meeks, H. K. Moffat, J. F. Grcar, and R. J. Kee, Sandia National Laboratories Report No. SAND96-8218, Albuquerque, NM (1996).
- ³⁵M. A. Lieberman and A. J. Lichtenberg, *Principles of Plasma Discharges and Materials Processing* (Wiley, New York, 1994).
- ³⁶M. E. Coltrin, R. J. Kee, F. M. Rupley, and E. Meeks, Sandia National Laboratories Report No. SAND96-8217, Albuquerque, NM (1996).
- ³⁷M. E. Coltrin, R. J. Kee, G. H. Evans, E. Meeks, F. M. Rupley, and J. F. Grcar, Sandia National Laboratories Report No. SAND91-8003, Albuquerque, NM (1991).
- ³⁸J. F. Grcar, Sandia National Laboratories Report No. SAND91-8230, Albuquerque, NM (1996).
- ³⁹J. T. Gudmundsson and M. A. Lieberman, *Plasma Sources Sci. Technol.* **7**, 1 (1998).
- ⁴⁰A. Kono, *Appl. Surf. Sci.* **192**, 115 (2002).